Restricted Trivariate Polycube Splines for Volumetric Data Modeling

Kexiang Wang, Xin Li, Bo Li, Huanhuan Xu, Hong Qin

Abstract—This paper presents a theoretical volumetric modeling framework to construct a novel spline scheme called restricted trivariate polycube splines (RTP-splines). The RTP-spline aims to generalize both trivariate T-splines and tensor-product B-splines, with a special emphasis on using solid polycube structure as underlying parametric domains and strictly bounded blending functions within such domains. Volumetric RTP-splines are uniquely constructed in a top-down fashion, through four major steps: (1) extending the polycube domain to its bounding volume via space filling; (2) building B-spline volume over the extended domain with restricted boundaries; (3) inserting duplicate knots through adding anchor points and performing local refinement; and (4) removing exterior cells and anchors. Besides local refinement inherited from general T-splines, our RTP-splines have the following attractive advantages: (a) naturally modeling solid objects with complicated topologies/bifurcations as a one-piece continuous representation without domain trimming/patching/merging, (b) guaranteed semi-standardness [1] so that the functions and derivatives evaluation is very efficient, (c) restricted support regions of blending functions, preventing control points from influencing other nearby domain regions that stay opposite to the immediate boundaries. These features are strongly desirable for certain applications such as isogeometric analysis. We conduct extensive experiments on converting complicated solid models into RTP-splines, and demonstrate the proposed spline to be a powerful and promising tool for volumetric modeling and other scientific/engineering applications where multi-attribute datasets are prevalent.

1 Introduction

Volumetric data of massive size are now available in a wide variety of scientific and research fields, because of the rapid advancement of modern data acquisition technologies. A frequently occurring problem is how to convert acquired 3D raw data of discrete samples into a continuous representation upon which simulation and analysis processes can be efficiently developed and accurately computed. The majority of traditional solid modeling techniques during the past four decades have been established upon the following theoretic foundations: constructive solid geometry (CSG), boundary representation (B-reps), and cell/space decomposition. Most of these representations lack the ability of smoothly modeling solid geometry, which is required by modern engineering design in order to directly apply physical simulations on modeled solids, without the necessity of expensive remeshing of finite-element structure and shape data conversion between discrete and continuous representations and between linear finite elements and higher piecewise splines in 3D. In practice, real-world objects (directly acquired via the scanning process) have complex geometries and non-trivial topologies. Therefore, constructing efficient representations for general solid objects in favor of physical simulation and engineering design remains to be a very challenging task. Trivariate simplex splines [2] have been developed to model multi-dimensional, material attributes of volumetric objects. However, computing blending functions and their derivatives on simplex splines is not straightforward and inefficient, compared with NURBS and tensor-product B-splines. Also, how to place boundary knots to avoid numerical degeneracies remains an open problem. Trivariate simplex splines are defined over an unstructured tetrahedral grid, which can be easily obtained from triangular meshes by certain mesh generation softwares such as *Tetgen* [3]. Although solid object of complex topologies and geometries can be modeled by trivariate simplex splines upon such unstructured grids, the majorities of simulation solvers have preferences on structured grid. This is because, low-quality tetrahedral meshes usually cause large simulation errors or numerical instability. Motivated by current industrial practice in various engineering design and analysis systems, we focus on designing a volumetric spline modeling framework based on structured grid domains.

In the framework of *isogeometric analysis* proposed by [4], [5], trivariate tensor-product B-splines/NURBS are directly used for modeling smooth geometry, material attributes, and physical simulation of solid objects simultaneously. Martin et al. [6] convert a solid femur mesh to a cylindrical trivariate B-spline by parameterizing the model into a solid cylinder. Due to the topological limitation of the cylinder domain, the constructed trivariate tensor-product splines can not model solid objects with bifurcations and arbitrary topologies, without enormous efforts in patch gluing/trimming, and imposing smoothness constraints along patch boundaries. Furthermore, local refinement required in level-of-detail modeling is not supported by tensor-product splines because basis function refinement will introduce many superfluous control points across the entire domain. As an extension to NURBS, T-splines [1], [7] solve this problem on semi-regular grid domains. To the best of our knowledge, no work has generalized T-splines for three dimensional, multi-attribute data and directly applied them to volumetric geometry and data modeling.

Directly generalizing T-spline surface to volumetric data is not straightforward. A general T-spline function defined

over a bivariate domain can be formulated as

$$\mathbf{F}(u,v) = \frac{\sum_{i=1}^{n} w_i \mathbf{p}_i B_i(u,v)}{\sum_{i=1}^{n} w_i B_i(u,v)} \quad (u,v) \in \mathbb{R}^2, \qquad (1)$$

where $\mathbf{p}_i$ are control points associated with weights w_i, and $B_i(u,v)$ denote basis functions. With this definition, two pieces of T-spline patches can be stitched together by blending boundary basis functions, and we form a new T-spline that can preserve smoothness across the boundary. Trivariate T-splines inherit such nice features, and T-splines defined on polycube volumetric domains can be similarly constructed by gluing a group of T-spline cubes. However, the calculation of this T-spline function and its derivatives requires to divide blending functions by the sum of all the contributed ones. This will make the evaluation computationally inefficient. Recently, *Semi-standard* T-splines introduced in [1] guarantee $\sum_{i=1}^{n} w_i B_i(u,v) \equiv 1$ in Eq (1) across the entire domain. In this setting, the computation of $\mathbf{F}(u,v)$ and its derivatives can be much more efficient.

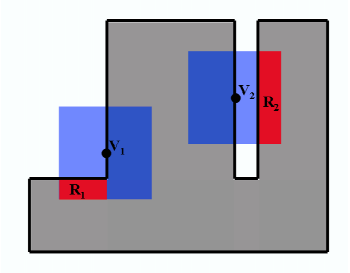

Fig. 1. Extra support regions. On a concave domain, if the supporting box of a blending function intersects with the domain boundary (e.g., boxes of v_1 and v_2), extra control points (e.g., in red regions) could contribute to the function blending unnecessarily.

However, how to construct a semi-standard T-spline, especially over non-trivial parametric domains, is a challenging problem. Another issue is that, conventional T-splines are defined with floating boundaries, i.e., the support regions of blending functions may go beyond the domain boundaries. Such a floating-boundary scheme upon a polycube domain will cause control points to unnecessarily contribute to extra domain regions. Two examples are shown as red-regions in Figure 1. This might cause geometric inconsistencies in modeling underlying solid objects, and in physical simulations. Therefore, it is ideal to have a trivariate spline inherit from T-splines, that (1) is defined within the largest visible region inside the domain, and (2) has the property of semi-standardness. Such novel splines will greatly facilitate direct modeling and physical simulations of arbitrary solid objects with complex geometries and sophisticated topologies. The spline constructed in this paper has these properties, and we call it the Restricted Trivariate Polycube Spline (RTP-spline).

This paper presents a framework of RTP-splines construction and the data conversion of volumetric models to this spline representation. It has major contributions:

- A new spline (RTP-spline) scheme is uniquely formulated over a polycube domain, with blending functions restricted inside the domain boundaries. The RTP-splines also have the following advantages: (1) It is capable of local refinement; (2) Computing RTP-spline functions and their derivatives is much more efficient than that on traditional T-spline surfaces; (3) The polycube domain enables natural modeling of arbitrary solid objects, since low distortions and few singularity points are introduced in volumetric parametrization when the domain mimics the geometries and topologies properly; (4) The restricted boundaries of the RTP-spline ensure the physical modeling and simulation adhere to geometry of underlying objects.
- We develop a novel framework to construct RTP-splines in an effective top-down fashion.
- We construct RTP-splines on several volumetric models with both geometry and synthesized textures (to mimic material properties), which demonstrates that our RTP-splines can model not only geometry but also multi-attribute fields within an unified paradigm.

The remainder of this paper is organized as follows. We review the related literature in Section 2, then introduce preliminaries and define necessary notations in Section 3. The methodology of RTP-spline construction is illustrated in Section 4. The entire process of converting discrete volumetric data into the spline representation is then explained in Section 5. We demonstrate experimental results in Section 6 and conclude the paper in Section 7.

2 Related Works

Research on spline-based volumetric modeling has gained much attention recently. 4D uniform rational cubic B-spline volume is used to constructively model FRep solids defined by real-valued functions [8]. The method presented in [9] represents and specifies physical attributes across a trivariate NURBS volume. However, it is more desirable in engineering design to have an integrated modeling framework that represents geometry, material attributes, and conducts simulations simultaneously. Trivariate NURBS are used to model skeletal muscle with anisotropic attributes [4], on which NURBS-FEM analysis is directly conducted. Martin et al. [6] present a method based on volumetric harmonic functions to parameterize a volumetric solid to a solid cylinder in order to fit a single trivariate B-spline to geometric data and model simulation attributes. A modeling technique based on triangular simplex splines [2] is developed to model and render multi-dimensional, material attributes for solid objects with complicated geometries and topologies.

The splines proposed in this paper are founded upon the T-spline technique [7]. T-splines are a generalization of NURBS, but permits T-junctions on its control mesh and enables local insertion of additional knots without introducing superfluous control points. A local refinement method is proposed in [1], [10] to simplify NURBS surfaces to T-spline representations by removing superfluous control points. The merge of B-spline patches defined over different local domains for getting a single T-spline representation on the manifold domain is thoroughly discussed in [11].

Bazilevs et al. [12] propose an isogeometric analysis framework based on T-splines. Its main focus is on planar T-splines for surfaces, and volumetric T-splines are only briefly mentioned without offering any technical details. Generalized trivariate T-splines (whose control points are associated with weights) are employed by [13] to model free-form deformation fields. For the purpose of shape metamorphosis, 3D level sets represented by T-splines are adopted in [14]–[17] for its efficiency. This is because, the distribution of T-spline control points can be made adaptive to the geometry of the morphing objects.

Our work relies on the construction and parameterization of a polycube domain. The parameterization on polycubes originated for seamless texture mapping with low distortion [18]. Polycubes serve as nice parametric domains because they approximate well the geometry of the model and possess great regularity. A polycube mapping can be constructed either manually [18]–[20] or automatically [21], [22]. Based upon specially-designed surface parametrization, [19] builds manifold bivariate T-spline over a polycube that can handle models with arbitrary topology. A few recent works [23]–[28] study the parameterization of a solid object to canonical domains such as spheres, polycubes, star-shaped volumes, etc. Volumetric parameterizations typically start from any given surface mapping, and parameterizing volumetric data onto a solid polycube domain serves as an important pre-processing step for the conversion of any solid model to RTP-splines.

3 Preliminaries and Notations

In this section, we introduce the general algorithm to construct trivariate T-spline with duplicate knots on a regular box domain, review the theory of basis function refinement, and define necessary notations for the rest of the paper.

3.1 Trivariate T-splines with Duplicate Knots

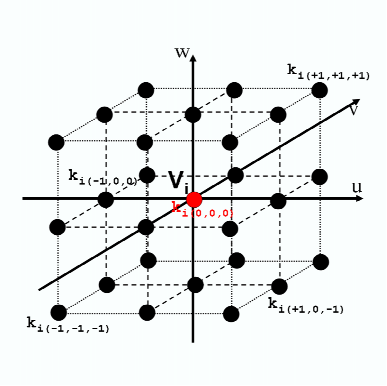

Fig. 2. A vertex $\mathbf{v}_i$ can have at most 27 anchors placed on $3 \times 3 \times 3$ virtual grids. The central one (red) is the master anchor and the rest (black) are sub-anchors.

Defined on a grid structure that allows T-junctions (or T-mesh), the T-spline proposed in [7] is a generalization of non-uniform B-splines (or NURBS). When considering a simple cube domain, the definition of T-spline surfaces can be straightforwardly extended to three dimensions and generate trivariate T-splines on T-lattice grids, where "T-junctions" are referred to the intersections between faces and/or lines.

Let $T(\mathcal{V}, \mathcal{C}, \mathcal{F})$ denote a rectilinear grid structure that permits T-junctions, where $\mathcal{V}$, $\mathcal{C}$, and $\mathcal{F}$ are sets of vertices, cells, and faces, respectively. $\mathcal{K} \subseteq \mathcal{V} \times \{-1, 0, +1\}^3$ denote a set of *anchors* attached to the vertices. At most 27 anchors are allowed at each vertex, and they can be imagined to be organized on a $3 \times 3 \times 3$ grid of infinitesimal size, as shown in Figure 2. We require that each vertex has a *master anchor* at the center of the local grid, while the others are optional and called *sub anchors*. In the rest of the paper, we denote an anchor at $\mathbf{v}_i$ as $\mathbf{k}_{i(\alpha,\beta,\gamma)}$, in which the triplet (α, β, γ) indicates a unique nodal position on the local grid. Given $\mathbf{v}_i = (v_i^0, v_i^1, v_i^2)$, all the corresponding anchors $\mathbf{k}_{i(\alpha,\beta,\gamma)}$ share the same coordinator (v_i^0, v_i^1, v_i^2) in parametric space. To distinguish these anchors for T-spline construction, we define $\bar{\mathbf{k}}_{i(\alpha,\beta,\gamma)} = \mathbf{v}_i + (\alpha, \beta, \gamma)\epsilon$ as the coordinator of $\mathbf{v}_{i(\alpha,\beta,\gamma)}$ in *construction space*, where ϵ is an infinitesimal with respect to the minimal cell size. In the rest of this paper, we sometimes represent an anchor by a simpler notation $\mathbf{k}_j$, where j indicates the index of $\mathbf{k}_{j(\alpha,\beta,\gamma)}$ in $\mathcal{K}$.

Given T and $\mathcal{K}$, a trivariate T-spline can be defined as

$$\mathbf{F}(u, v, w) = \frac{\sum_{i=1}^{|\mathcal{B}|} \mathbf{p}_i B_i(u, v, w)}{\sum_{i=1}^{|\mathcal{B}|} B_i(u, v, w)} \quad (u, v, w) \in \mathbb{R}^3, \quad (2)$$

where (u, v, w) denotes 3D parametric coordinates, $\mathbf{p}_i$ are control points, and $\mathcal{B} = \{B_i(u, v, w)\}$ is the collection of blending functions. Each $B_i(u, v, w)$ is a tensor-product of three B-spline basis functions, written as

$$B_i(u, v, w) = N_{i0}^3(u) N_{i1}^3(v) N_{i2}^3(w), \quad (3)$$

where $N_{i0}^3(u)$, $N_{i1}^3(v)$ and $N_{i2}^3(w)$ are defined along u, v, and w directions, respectively. In the case of cubic T-spline, the univariate function N_{ij}^3 is constructed upon the knot vector $\Xi_i^j = [\xi_{i0}^j, \xi_{i1}^j, \xi_{i2}^j, \xi_{i3}^j, \xi_{i4}^j]$, which is deduced from T and a collection of anchors $\mathcal{K}$.

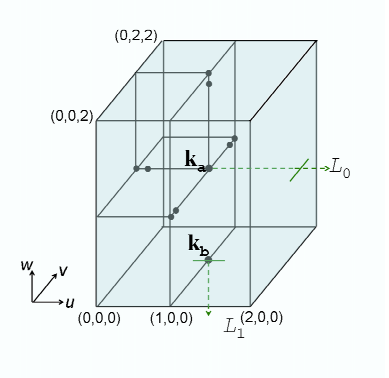

Fig. 3. Knot vectors are derived from a T-lattice associated with a set of anchors (dots). The knot vector from $\mathbf{k}_a$ is $[0, 0, 1, 2, 2]$ in $+u$ direction, where 2 repeats twice because L_0 intersects once with the rightmost boundary. The knot vector from $\mathbf{k}_b$ toward $-w$ direction has 0 repeated three times because L_1 intersects nothing from T or $\mathcal{K}$ except $\mathbf{k}_b$.

We refer the knot vector in construction space by notation $\Xi_i^j = [\bar{\xi}_{i0}^j, \bar{\xi}_{i1}^j, \bar{\xi}_{i2}^j, \bar{\xi}_{i3}^j, \bar{\xi}_{i4}^j]$ for the rest of the paper, unless mentioned otherwise. In the case of cubic T-splines, each blending function must be associated with an anchor, which coincides with the middle knot of its three knot vectors.

To infer knot vectors from a T-lattice is parallel to that for T-mesh, except that the searching is conducted in construction space. Starting from an anchor $\bar{\mathbf{k}} = (\bar{\xi}_{i2}^0, \bar{\xi}_{i2}^1, \bar{\xi}_{i2}^2)$, $\bar{\xi}_{i3}^0$ and $\bar{\xi}_{i4}^0$ are found by shooting a ray $L(t) = (\bar{\xi}_{i2}^0 + t, \bar{\xi}_{i2}^1, \bar{\xi}_{i2}^2)$ into construction. ξ_{i3}^0 and ξ_{i4}^0 are the corresponding coordinate values at the first two intersections where $L(t)$ comes across either an anchor or a face in $\mathcal{F}$. If $L(t)$ does not make two intersections before shooting outside T, the last coordinate value is repeated, *e.g.*$\xi_{i3}^0 = \xi_{i4}^0$ or $\xi_{i2}^0 = \xi_{i3}^0 = \xi_{i4}^0$ (see Figure 3). The knots in other directions are determined in a similar fashion.

3.2 Refinement of B-spline Functions

To refine blending functions on trivariate T-splines, we need to review the knot insertion algorithm for univariate B-spline functions. Let $\Xi = [\xi_0, \xi_1, \xi_2, \xi_3, \xi_4]$ be a knot vector and $N(\xi)$ denote the cubic B-spline basis function defined on it. If there is an additional knot $k \in [\xi_0, \xi_4]$ inserted into Ξ, $N(\xi)$ can be written as a linear combination of two scaled B-spline functions as

$$N(\xi) = c_1 N_1(\xi) + c_2 N_2(\xi), \tag{4}$$

where c_1, c_2 and knot vectors for $N_1(\xi)$ and $N_2(\xi)$, determined by the rules in Table 1.

4 Constructing RTP-splines

The construction of RTP-splines includes four major steps (see Figure 4): (1) extending given polycube P domain to a box domain, (2) building trivariate B-splines with restricted boundaries, (3) introducing duplicate knots by inserting additional anchors, and performing local refinement to separate interior and exterior blending functions, and (4) producing RTP-splines by removing structures/anchors outside P. These steps are discussed in the following four subsections respectively.

4.1 Extending Polycubes to Bounding-Boxes

Following the notations introduced in Section 3.1, on the trivariate T-spline domain, let $P = (\mathcal{V}^P, \mathcal{C}^P, \mathcal{F}^P)$ be a given polycube structure, where $\mathcal{V}^P$, $\mathcal{C}^P$ and $\mathcal{F}^P$ denote vertices, cubes and cell faces respectively. In order to extend P to a box volume with rectilinear grids, P should not have T-junctions or intersections between its cell faces. Our parametric polycube domains (see Section 5.1) do not contain T-junctions. If other polycube mapping methods are used to construct the parametric domain and the generated domain has T-junctions, then we can always eliminate them simply by splitting the cells across the domain, through the extended planes of these intersecting cell faces. Now P can be extended to its bounding-box domain $T(\mathcal{V}, \mathcal{C}, \mathcal{F})$ by filling in some solid cuboid structures $G = (\mathcal{V}^G, \mathcal{C}^G, \mathcal{F}^G)$, where $\mathcal{V}^G = \mathcal{V} - \mathcal{V}^P$, $\mathcal{C}^G = \mathcal{C} - \mathcal{C}^P$, $\mathcal{F}^G = \mathcal{F} - \mathcal{F}^P$. G represents the exterior structure of P and we call its domain the *ghost region*. Note that there is a rectilinear grid embedded in the space of T, and the grids coordinates in k-axis direction are represented by

$$\mathbf{S}_k = [s_1^k, s_2^k, \ldots, s_{n_k}^k] \quad k = 1, 2, 3$$

where n_k is the resolution of rectilinear grid along k-axis.

4.2 Building the B-spline Volume with Restricted Boundary

With the bounding box domain T constructed, it is not difficult to construct a trivariate tensor-product B-spline from the rectilinear grid structure on T by using $\mathbf{S}_1$, $\mathbf{S}_2$ and $\mathbf{S}_3$. We must augment $\mathbf{S}_k$ to have a valid B-spline definition that covers the entire domain T. One method is to add extra knots outside the domain region, generating a floating-boundary scheme. In this paper, we duplicate the knots at both ends of $\mathbf{S}_k$ in order to restrict the B-spline blending function within the domain T, i.e., $\mathbf{S}_k$ turns into

$$\mathbf{S}_k = [s_1^k, s_1^k, s_1^k, s_1^k, s_2^k, \ldots, s_{n_k-1}^k, s_{n_k}^k, s_{n_k}^k, s_{n_k}^k, s_{n_k}^k]$$

in which 3 extra knots are added to each end. Therefore, the trivariate tensor-product B-spline defined on T is formulated as

$$\mathbf{F}(u, v, w) = \sum_{i=1}^{n} \mathbf{p}_i B_i(u, v, w) \quad (u, v, w) \in \mathbb{R}^3 \tag{5}$$

where $n = (n_1 + 2) \times (n_2 + 2) \times (n_3 + 2)$ is the number of control points, and $B_i(u, v, w)$ are blending functions defined in Equation (3).

Alternatively, we can obtain $\mathbf{F}$ by constructing blending functions similar to T-splines (Section 3.1, instead of computing them from 3 global knot vectors. We let $\mathcal{S} = \{s_1^0, s_1^0 + \epsilon, \ldots, s_{n_0}^0 - \epsilon, s_{n_0}^0\} \times \{s_1^1, s_1^1 + \epsilon, \ldots, s_{n_1}^1 - \epsilon, s_{n_1}^1\} \times \{s_1^2, s_1^2 + \epsilon, \ldots, s_{n_2}^2 - \epsilon, s_{n_2}^2\}$ and choose the anchor set $\mathcal{K} = \{\bar{\mathbf{k}}_{i(\alpha,\beta,\gamma)} \,|\, \bar{\mathbf{k}}_{i(\alpha,\beta,\gamma)} \in \mathcal{S}\}$, then build blending functions associated with each anchor. $\mathcal{K}$ contains sub anchors that only exist at corner, edge, and face vertices (see their configurations in Fig 5(a)). These sub anchors guarantee partition-of-unity of $\mathbf{F}$ and limit the influential regions of blending functions within the domain T.

4.3 Local Refinement and Anchor Insertion

Let internal and ghost blending functions refer to the blending functions associated with anchors in P and G respectively. In this section, we seek to refine existing blending functions with knot insertion and local refinement, so that the resulting internal and ghost blending functions are isolated and restricted boundary forms along the surface of P. More precisely, our goal is to enforce the following rules to the blending function set:

(i) No ghost blending function influences any part of the polycube domain.
(ii) Semi-standardness is preserved on the internal blending function set even if G and all the ghost anchors are removed.
(iii) No internal blending function influences any region outside the polycube domain if G and all the ghost anchors are removed.

TABLE 1
Refinement of $N(\xi)$ by inserting k into knot vector $[\xi_0, \xi_1, \xi_2, \xi_3, \xi_4]$, which generates two basis functions $N_1(\xi)$ and $N_2(\xi)$, scaled by c_1 and c_2 respectively.

k	c_1	c_2	knot vector of $N_1(\xi)$	knot vector of $N_2(\xi)$
$\xi_0 \le k < \xi_1$	$\frac{k-\xi_0}{\xi_3-\xi_0}$	1	$[\xi_0, k, \xi_1, \xi_2, \xi_3]$	$[k, \xi_1, \xi_2, \xi_3, \xi_4]$
$\xi_1 \le k < \xi_2$	$\frac{k-\xi_0}{\xi_3-\xi_0}$	$\frac{\xi_4-k}{\xi_4-\xi_1}$	$[\xi_0, \xi_1, k, \xi_2, \xi_3]$	$[\xi_1, k, \xi_2, \xi_3, \xi_4]$
$\xi_2 \le k < \xi_3$	$\frac{k-\xi_0}{\xi_3-\xi_0}$	$\frac{\xi_4-k}{\xi_4-\xi_1}$	$[\xi_0, \xi_1, \xi_2, k, \xi_3]$	$[\xi_1, \xi_2, k, \xi_3, \xi_4]$
$\xi_3 \le k \le \xi_4$	1	$\frac{\xi_4-k}{\xi_4-\xi_1}$	$[\xi_0, \xi_1, \xi_2, \xi_3, k]$	$[\xi_1, \xi_2, \xi_3, k, \xi_4]$

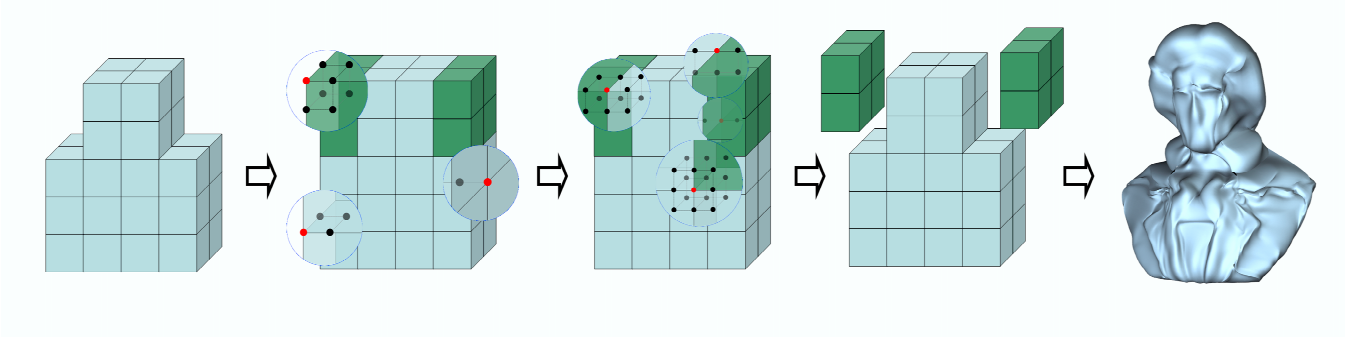

Fig. 4. Overview of 4-step RTP-spline Construction Pipeline. (1) Extend polycube domain to its bounding-box; (2) build B-spline volume with bounded boundaries, (3) insert anchors and refine blending functions, (4) remove exterior regions.

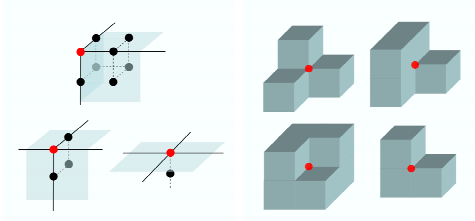

(a) (b)

Fig. 5. (a) Knot configuration at corner, edge and face vertices for restricted boundaries. (b) Examples of extraordinary corners on a polycube.

To achieve this goal, we systematically add new anchors in two steps. First, add sub-anchors at the polycube boundary vertices (Section 4.3.3). Second, keep inserting sub-anchors to refine those blending functions that violate the above rules, until there exist no violations. Adding new sub-anchors ultimately introduces duplicate knots into knot vectors, which serves for two purposes: (1) reducing the influential region of a blending function and (2) degenerating the continuity of a blending function to C^0 at desired places (Section 4.3.2). Moreover, as new anchors may lead to disagreements between existing blending functions and underlying knot vectors implied by T and new $\mathcal{K}$, an algorithm (Section 4.3.1) is necessary to resolve these inconsistencies after new anchors have been inserted.

4.3.1 Local Refinement of Blending Functions

We need to introduce an algorithm to update blending functions $\mathcal{B}$ accordingly, once there occurs any change in the anchor set $\mathcal{K}$ and/or the domain structure T. The refinement algorithm proposed in [1], [10] is designed for surface editing, the primary goal of which is to preserve the shape of a T-spline surface whenever new control points are inserted. In this paper, we extend this algorithm to 3D and enhance it to support trivariate T-spline with duplicate knots. By interpreting the B-spline volume previously obtained as a general trivariate T-spline, we can rewrite its representation from Equation 5 to

$$\mathbf{F}(u,v,w) = \frac{\sum_{i=1}^{|\mathcal{B}|} w_i \mathbf{p}_i B_i(u,v,w)}{\sum_{i=1}^{|\mathcal{B}|} w_i B_i(u,v,w)} \quad (u,v,w) \in \mathbb{R}^3 \quad (6)$$

where w_i is the weight associated with each blending function B_i. Note that the T-spline so far is essentially a B-spline volume: $\sum_{i=1}^{|\mathcal{B}|} w_i B_i(u,v,w) \equiv 1$ for any (u,v,w) and $w_i = 1$ for any i.

Let $\mathcal{K}^*$ denote the updated anchor set and $T^*(\mathcal{V}^*, \mathcal{C}^*, \mathcal{F}^*)$ be the new grid structure after vertex insertion or cell splitting. Given $\mathcal{K}^*$, T^*, $\mathcal{W}$ and $\mathcal{B}$, Algorithm 1 generates new blending function set $\mathcal{B}^*$ and new weights $\mathcal{W}^*$ accordingly, along with updated $\mathcal{K}^*$ and $\mathcal{T}^*$.

In Algorithm 1, the superscript indicates the index of the original blending function from $\mathcal{B}$, with which a variable is associated, and the subscript indicates the index of the associated central anchor. For example, B_i^t is a blending function associated with anchor $\mathbf{k}_i$ and originates from the t-th blending function from $\mathcal{B}$. The star superscript indicates that the variables are obtained from the modified domain T^*, *e.g.*, Ξ_i^* denotes the knot vectors deduced from T^* and *centered* at $\mathbf{k}_i^*$ (*i.e.*, the three middle knots of Ξ_i^* coincide with $\mathbf{k}_i^*$).

The basic idea of Algorithm 1 is as follows. First, we decouple blending functions from T and $\mathcal{K}$. Then, by either inserting new anchors or refining basis functions (Section 3.2), we keep resolving the inconsistencies between $\mathcal{B}$ and the local knot vectors implied by $\mathcal{K}^*$ and

Algorithm 1: small Refinement of trivariate T-spline blending functions in support of duplicate knots.

Input: $T^*(\mathcal{V}^*, \mathcal{C}^*, \mathcal{F}^*)$, $\mathcal{K}^*$, $\mathcal{B}$ and $\mathcal{W}$.
Output: T^*, $\mathcal{K}^*$, $\mathcal{B}^*$ and $\mathcal{W}^*$
s.t. $\sum_{i=1}^{|\mathcal{B}^*|} w_i^* B_i^* \equiv \sum_{i=1}^{|\mathcal{B}|} w_i B_i$

$Q \Leftarrow \{(w_i^i, B_i^i) : w_i \in \mathcal{W}, B_i \in \mathcal{B}\}$
while $\exists (w_i^t, B_i^t) \in Q : \Xi_i^t \neq \Xi_i^*$ *in parametric space* **do**
  forall the $(w_i^t, B_i^t) \in Q$ **do**
    infer the knot vectors Ξ_i^* *centered* at $\mathbf{k}_i^*$ from T^*
    if $\Xi_i^t = \Xi_i^*$ *in parametric space* **then**
      $\Xi_i^t \Leftarrow \Xi_i^*$
    else if Ξ_i^* *is more refined than* Ξ_i^t **then**
      insert a knot of Ξ_i^* not existing in Ξ_i^t into Ξ_i^t, add the relative anchor and do the refinement: $B_i^t = c_1 \tilde{B}_j^t + c_2 \tilde{B}_i^t$ (Section 3.2)
      $\tilde{w_j^t} \Leftarrow w_i^t \cdot c_1; \quad \tilde{w_i^t} \Leftarrow w_i^t \cdot c_2$
      $Q \Leftarrow Q - \{(w_i^t, B_i^t)\} \cup \{(\tilde{w_j^t}, \tilde{B_j^t}), (\tilde{w_i^t}, \tilde{B_i^t})\}$
    else if Ξ_i^t *indicates an anchor* $\mathbf{k}_{j(\alpha,\beta,\gamma)} \notin \mathcal{K}^*$ **then**
      $\mathcal{K}^* \Leftarrow \mathcal{K}^* \cup \mathbf{k}_{j(\alpha,\beta,\gamma)}$
      if $\mathbf{k}_{j(0,0,0)} \notin \mathcal{K}^*$ **then**
        $\mathcal{K}^* \Leftarrow \mathcal{K}^* \cup \{\mathbf{k}_{j(0,0,0)}\}$
        $\mathcal{V}^* \Leftarrow \mathcal{V}^* \cup \{\mathbf{v}_j\}$ `// Insert a new vertex`
      end if
    end if
  end forall
  forall the $c \in \mathcal{C}^*$ **do**
    if *vertices on the edges of* c *form an axis-aligned plane that splits* c *into* c_1 *and* c_2 **then**
      $\mathcal{C}^* \Leftarrow \mathcal{C}^* - \{c\} \cup \{c_1, c_2\}$ `// divide` c `into` c_1 `and` c_2
    end if
  end forall
end while
$\mathcal{B}^* \Leftarrow \{B_i : (w_i^t, B_i^t) \in Q\}$
$\mathcal{W}^* \Leftarrow \{w_j = \sum_{\forall (w_j^t, B_j^t) \in Q} w_j^t\}$

$\mathcal{T}^*$. A cell splits into half if there are vertices on its edges forming an axis-aligned plane. Finally, any blending functions arising from different refinements but having equivalent knot vectors in parametric space are merged into a single one with their weights being summed.

Note that any blending function introduced by Algorithm 1 must center at a certain anchor, but not vice versa, *i.e.*, there could be anchors not associated with any blending functions. Moreover, the new T-spline after refinement is still semi-standard, because the denominators in Equation 6 remain unchanged in Algorithm 1, due to

$$w_i^t B_i^t \equiv w_i^t \cdot c_1 B_j^t + w_i^t \cdot c_2 B_i^t \equiv \tilde{w_j^t} \tilde{B_j^t} + \tilde{w_i^t} \tilde{B_i^t}$$

4.3.2 Modifying Blending Functions with Anchor Insertions

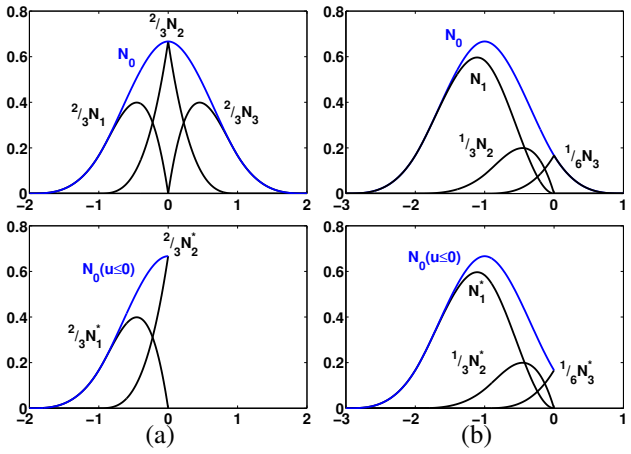

Fig. 6. Examples of eliminating violations against rules (i)(ii) in the case of cubic B-spline basis functions. Suppose $x = 0$ is the boundary and the ghost region covering $(0, \infty)$ in (a), N_0 represents an internal basis against (ii). After two extra knots 0 are inserted, N_0 is refined to N_1 and N_2 which comply with rule (ii); In (b) where the ghost region covers $(-\infty, 0)$, ghost basis N_0 violates the rule (i). After refinement with insertion of duplicate knots, it is replaced by N_1 and N_2 in ghost blending functions. Thus, no violation against (i) exists.

The anchor operation is our fundamental tool to modify existing blending functions of trivariate T-splines in order to get rid of all violations against rules (i), (ii) and (iii). As blending functions of trivariate T-splines are tensor-products of three univariate cubic B-spline bases, let's expose this method in 1D by using two examples given in Figure 6. In Figure 6(a), $N_0 = N[-2, -1, 0, 1, 2]$ represents an internal basis which apparently violates rule (ii). If two extra knots 0s are inserted, N_0 is refined into two internal bases $N_1 = N[-2, -1, 0, 0, 0]$ and $N_2 = N[-1, 0, 0, 0, 1]$, one ghost basis $N_3 = N[0, 0, 0, 1, 2]$, such that $N_0 = \frac{2}{3}N_1 + \frac{2}{3}N_2 + \frac{2}{3}N_3$ according to the refinement algorithm in Section 3.2. Now once the ghost region is gone, N_1 and N_2 change to $N_1^* = N[-2, -1, 0, 0, 0]$ and $N_2^* = N[-1, 0, 0, 0, 0]$ respectively and we still have $N_0(u) = \frac{2}{3}N_1^*(u) + \frac{2}{3}N_2^*(u)$ on $u \in [-2, 0]$, as shown in the bottom of Figure 6(a). Therefore, the violation against (ii) is successfully eliminated. Figure 6(b) depicts a scenario where $N_0 = N[-3, -2, -1, 0, 1]$ in violation of rule (i) overlaps with the domain region at $[0, 1]$. By inserting two duplicate knots at 0, we may replace N_0 with two resulting ghost bases N_1 and N_2, both of which abide with the rule (i). For the case of trivariate T-splines, knot insertions are replaced by anchor insertions conducted on T-lattice, and a much more complex refine algorithm (see Section 4.3.1) is employed instead.

4.3.3 Anchor Insertions on Polycube Boundary

It's easy to see that the blending functions associated with those master anchors either on, or adjacent to the interfaces

between P are G are in violation of rule (ii). Therefore, we need to insert sub-anchors to boundary vertices. The basic idea is analogous to that in Section 4.2 where sub-anchors are added on the surface of a box domain to ensure its restricted boundary. However, a variety of corner types may be found on polycube surfaces (see Figure 5(b)), thus we have to handle all of them for proper anchor insertions. To exhaust all possible corner types, then choose sub-anchors to insert is tedious and inefficient. Instead, we developed a general algorithm to determine which sub-anchors to be inserted at arbitrary boundary vertex. Given a boundary vertex $\mathbf{v}_i$, we first add the master anchor to it, along with all the sub-anchors that lie within the domain of T in construction space. Then the sub-anchors lying within the domain of P in construction space are colored red, and the others are blue. If there exists $\mathbf{k}_{i(-\alpha,\beta,\gamma)} \in \mathcal{K}$ for all $\mathbf{k}_{i(\alpha,\beta,\gamma)} \in \mathcal{K}$ and $color(\mathbf{k}_{i(-\alpha,\beta,\gamma)}) = color(\mathbf{k}_{i(\alpha,\beta,\gamma)})$ for $\alpha \in \{-1,1\}$ $\beta,\gamma \in \{-1,0,1\}$, we delete $\{\mathbf{k}_{i(\pm 1,\beta,\gamma)}\}$ from $\mathcal{K}$, that is, the sub-anchors on the 1st and the 3rd layers in 0-axis direction of the $3\times3\times3$ grid at $\mathbf{v}_i$ match in color pattern, they are deleted from $\mathcal{K}$. Then this operation is performed similarly in the other directions. The intuition of this method is to generate C^0 continuities at the boundaries with as few sub-anchors as possible, in order to keep the smoothness along the other directions. An example is given in Figure 7 in which sub-anchors are inserted at a boundary vertex on a 2D mesh. After all the required sub-anchors are added at the interface between P and G, Algorithm 1 is then applied to generate a new set of blending functions and a new set of weights.

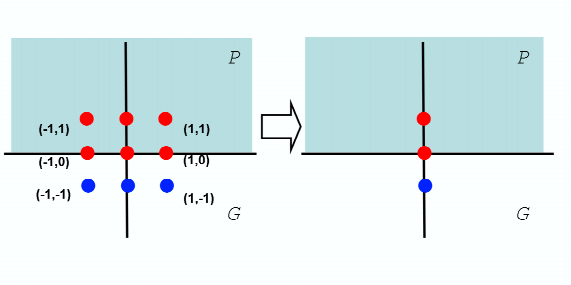

Fig. 7. Inserting sub-anchors to a boundary vertex. Red dots denote anchors inside P and blue ones are those in G. As the color patterns on the leftmost and rightmost grid layer match, all sub-anchors on both layers are removed.

4.3.4 Other Anchor Insertions

Section 4.3.3 has resolved most violations against rules (i) and (ii) arising from the blending functions that are associated with the master anchors close to the polycube boundary. Nevertheless, there are still other violations left. They can be categorized into four types as follows

1) (see Figure 8(a)) Ghost blending functions associated with sub-anchors violate rule (i). For example, the support region of the blending function associated with $\mathbf{k}_{i(1,0)}$ (the other index is omitted for conciseness reason) overlaps with P. A pair of anchors $\mathbf{k}_{a(1,1)}$ and $\mathbf{k}_{a(1,-1)}$ can be added to reduce the support region to the boundary while no further violations being introduced. The violation arising from $\mathbf{k}_{j(1,-1)}$ is treated in the same fashion. In the case of $\mathbf{k}_{k(1,1)}$, only 1 sub-anchor $\mathbf{k}_{k(1,-1)}$ is required to eliminate the violation.
2) (see Figure 8(b)) Internal blending functions associated with sub-anchors violate rule (ii). For example, removal of the ghost region and ghost anchors will cause the changes in the shape of the blending function associated with $\mathbf{k}_{i(1,0)}$ because its knot vector goes into the ghost region. Similar to case 1, $\mathbf{k}_{a(1,1)}$ and $\mathbf{k}_{a(1,-1)}$ can be added to cut off the blending function from outside. Only one anchor insertion is necessary to resolve the violation arising from $\mathbf{k}_{j(1,-1)}$. Even though the new blending functions after refinement still covers nearby ghost region, it doesn't violate rule (ii) anymore. This has been explained in Section 4.3.2 (Figure 6(a)).
3) (see Figure 8(c). We illustrate four different separate cases together in (c). Thus we consider the existence of only one blue anchor each time.) Ghost blending functions near a convex corner of P violate rule (i). For example, in spite of its knot vectors being apart from P and any internal anchors, the blending function associated with $\mathbf{k}_{a(0,0)}$ still influence the internal corner region. To remedy this violation, two sub-anchors $\mathbf{k}_{c(1,0)}$ and $\mathbf{k}_{b(0,1)}$ are added to the extended surfaces of the convex corner, shrinking the support region of the blending function centered at $\mathbf{k}_{a(0,0)}$ via refinement to separate it from P. Similarly, $\mathbf{k}_{c(1,0)}$ and $\mathbf{k}_{b(-1,1)}$ are added for $\mathbf{k}_{a(-1,0)}$, $\mathbf{k}_{c(1,-1)}$ and $\mathbf{k}_{b(0,1)}$ for $\mathbf{k}_{a(0,-1)}$ and $\mathbf{k}_{c(1,-1)}$ and $\mathbf{k}_{b(-1,1)}$ for $\mathbf{k}_{a(-1,-1)}$.
4) (see Figure 8(d). There are also four independent cases presented in (d).) Internal blending functions near a concave corner of P violate rule (iii). This type of violation is similar to case 3 except that the domain region and the ghost regions are interchanged and the purpose of eliminating this kind of violations is to ensure restricted boundary of P.

Once new sub-anchors are inserted for all violations, we apply the refinement algorithm given in Section 4.3.1 and obtain new sets of blending functions, weights and anchors along with the updated T-lattice structures. Since extra anchors may be introduced by the refinement, we have to search for new violations and resolve them again. These two steps are repeated until no violation is found. We notice in our experiment that it only takes one or two iterations in practice to eliminate all violation cases. On the other hand, the proposed anchor insertion method is guaranteed to terminate due to the fact that no vertex is added during refinement, and there are only a finite number of sub-anchors that can be added to T. In the worst case, each cube of T turns into a small Bézier volume.

4.4 Generating RTP-spline Function

By removing G and all ghost anchors from $\mathcal{K}$, we obtain a RTP-spline, a single-piece smooth function, defined

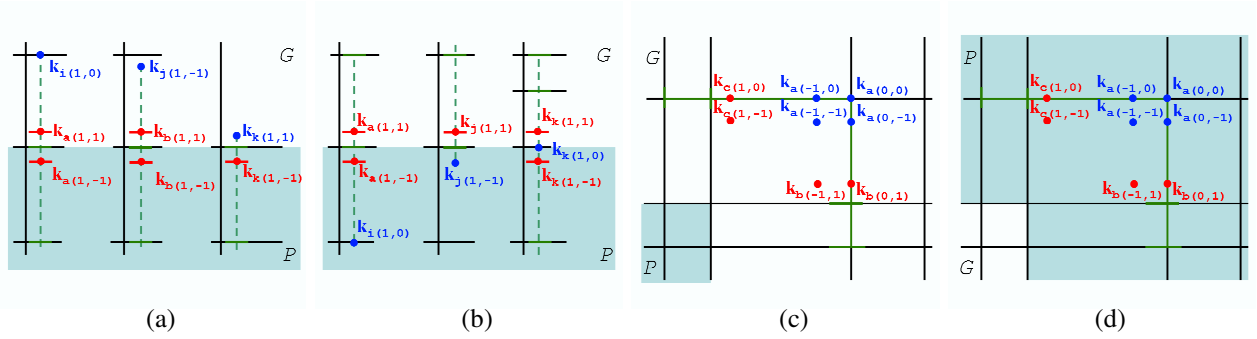

Fig. 8. Violation cases. The blue dots represent the associated anchors of violating blending functions. The anchors added to remedy the corresponding violations are colored red. (a) and (c) show the violation cases against rule (i); (b) shows the cases against rule (ii); (d) shows the cases against rule (iii). Note that in (c), we illustrate four independent violation cases in one figure. In (d), we also show four independent cases.

over a polycube domain P. Our anchor insertion method guarantees that the resulting RTP-splines have a restricted boundary. Furthermore, the refinement algorithm proposed in Section 4.3.1 ensures semi-standardness of the obtained RTP-splines from the original B-spline volume. Since the denominator remains 1 over the entire domain P, we can rewrite Equation 6 in a simpler formulation:

$$\mathbf{F}(u,v,w) = \sum_{i=1}^{|\mathcal{B}|} w_i \mathbf{p}_i B_i(u,v,w) \quad (u,v,w) \in \mathbb{R}^3 \qquad (7)$$

5 Modeling Solid Objects

It is a challenging task to build single-piece and smooth spline representations for arbitrary solid objects, especially for those with bifurcations and high genus. This section addresses how to construct a RTP-spline for a given solid model. In this work, an input solid model is represented as a dense tetrahedral mesh $M = \{\mathcal{V}, \mathcal{T}\}$. Its geometry and other material attributes are discretely represented on vertices $\mathcal{V}$, and are interpolated linearly within each tetrahedron of $\mathcal{T}$. Note that our volumetric mapping algorithm is a meshless method with a closed-form mapping representation, and it works for other volumetric data representations such as point clouds and voxel grids. Therefore, the entire RTP spline construction pipeline can be easily generalized to handle other volumetric data input formats.

We first construct a polycube P following the geometry and topology of M and compute a volumetric mapping $\mathbf{f} : P \to M$ (see Section 5.1), then construct a RTP-spline function $\mathbf{F}(u,v,w)$ over the polycube domain P (with the algorithm proposed in Section 4), and finally fit it to a group of data point chosen from M.

5.1 Parameterization on Polycube Domains

Computing volumetric parameterizations is an important issue for the RTP-spline construction. Tensor-product trivariate splines usually need to be defined over a parametric (box) domain, and the quality of the parameterization can affect the fitting efficacy of splines. Therefore, we choose to use the polycube parametric domain which possesses great regularity while well approximates the geometry of the original object.

A volumetric parameterization of a solid model M embedded in $\mathbb{R}^3$ on a polycube P is a bijective mapping $\mathbf{f} : P \to M, P, M \subset \mathbb{R}^3$. The polycube P can be constructed either manually [19], [20], [29] or automatically [21], [22]. These techniques also provide the boundary mapping $\mathbf{g}$ from the polycube boundary surface (denoted as ∂P) to the boundary of M (∂M). We use such a surface mapping $\mathbf{g} : \partial P \to \partial M$ as the boundary condition of $\mathbf{f}$. The volumetric parameterization is then defined as the seeking of a harmonic energy minimizer:

$$\begin{cases} \Delta \mathbf{f}(\mathbf{x}) = 0 & \mathbf{x} \in P, \\ \mathbf{f}(\mathbf{x}) = \mathbf{g}(\mathbf{x}) & \mathbf{x} \in \partial P. \end{cases}$$

where Δ is the 3-dimensional Laplace operator, defined for each real function f in $\mathbb{R}^3$ as

$$\Delta f = \nabla \cdot \nabla f = \frac{\partial^2 f}{\partial x^2} + \frac{\partial^2 f}{\partial y^2} + \frac{\partial^2 f}{\partial z^2}.$$

$\Delta \mathbf{f} = 0$ for $\mathbf{f} = (f^1, f^2, f^3)$ is equivalent to $\Delta f^i = 0$ in all the $i = 1, 2, 3$ coordinate directions. We compute the volumetric polycube mapping using the method of fundamental solutions (MFS) [24], [30]. We recap the basic algorithm here and refer more details to [24].

Based on the maximum principal of harmonic functions, critical points of harmonic functions exist only on the boundary. Furthermore, function values in the interior region of P are fully determined by the boundary values $f(\mathbf{x}), \mathbf{x} \in \partial P$ and can be computed by Green's functions. Specifically, the real harmonic function value $f(\mathbf{x})$ can be computed as the integration of its boundary values and the kernel function (i.e. fundamental solutions associated with the 3D Laplacian operator Δ). The kernel function of Δ has the following formula:

$$K(\mathbf{x}, \mathbf{x}') = \frac{1}{4\pi} \frac{1}{|\mathbf{x} - \mathbf{x}'|},$$

which matches the electrostatistics. In other words, solving a harmonic function can be converted to designing a specific electric field determined by an electronic particle

system, whose electric potential mimics f and shall satisfy the boundary condition $\mathbf{g}$ on ∂P.

The computation pipeline is to first place a set of charge points $\{q_s\}$ outside the domain $q_s \in \partial\widetilde{P}, P \subset \widetilde{P} \subset \mathbb{R}^3$. Then we conduct a boundary fitting which solves the charge distribution $\{w_s\}$ on these points $\{q_s\}$. The harmonic function $f(x)$ is represented using the MFS equation:

$$f(\mathbf{x}, W, Q) = \sum_{s=1}^{N_s} w_s \cdot K(\mathbf{x}, q_s), \mathbf{x} \in P, q_s \in \partial\widetilde{P},$$

where f is guaranteed to be harmonic, and we only need to enforce the boundary condition on ∂P. For the boundary fitting, we sample N_c collocation points on the domain boundary ∂P to set up the constraint equations. If we have N_s charge points and N_c collocation points, for a real harmonic function f (e.g. on an individual axis direction) we only need to solve an $Ax = b$ linear system where A is an $N_c \times N_s$ matrix. The system can be efficiently solved by a truncated Singular Value Decomposition [24], [31].

The parametrization of a general solid model on its adaptive polycube domain can get lower distortion than that on a single box domain, since the polycube can be constructed to have the same topology and similar geometry as the model. Actually, in RTP-spline construction, the parameterization without fully conformality and equivolume-property does not bring too much trouble to the volume fitting, as long as the overall parametrization mapping is continuous and smooth. Therefore, the current parameterization is efficient and sufficient, i.e. the shape (angle) distortion and volume distortion of our volumetric mapping are satisfactory.

Along two directions, we will also explore volumetric mapping techniques for parameterization with higher quality: (1) we can use more complicated/general parametric domains such as manifold domains (directly represented by tetrahedral meshes), polytubes [29], and so forth, which may more flexibly approximate the shape and yield lower distortion. However, on such domains it becomes more challenging to construct regular splines providing same favorable features of RTP-splines. (2) the current volumetric mapping is fully determined by the boundary constraint, i.e., the polycube surface mapping [19]. We can reduce the distortion by conducting relaxation of boundary surface mapping [32], now driven by the volumetric mapping distortion. However, this makes the mapping computation a nonlinear optimization which is inefficient.

5.2 RTP-spline Volume Fitting

Given $\mathbf{f} : P \to M$, we evenly select a group of points $U = \{\mathbf{u}_1, \mathbf{u}_2, \ldots, \mathbf{u}_m\}$ from the polycube parametric domain p, hence their counterparts in the real world domain are $X = \{\mathbf{x}_i = \mathbf{f}(\mathbf{u}_i), i = 1, \ldots, m\}$. The problem of fitting the RTP-splines $\mathbf{F}(u, v, w)$ resorts to minimizing the following equation using U and X, with respect to control points $\mathbf{p}_i$

$$\sum_{i=1}^{m} (\mathbf{F}(\mathbf{u}_i) - \mathbf{x}_i)^2 \tag{8}$$

Alternatively, it can be represented in format of

$$\frac{1}{2}\mathbf{P}^T\mathbf{B}^T\mathbf{B}\mathbf{P} - \mathbf{X}^T\mathbf{B}\mathbf{P} \tag{9}$$

in which $\mathbf{P}_j = \mathbf{p}_j^T$, $\mathbf{X}_i = \mathbf{x}_i^T$, and $\mathbf{B}_{ij} = \mathbf{I}_{3\times3}B_i(\mathbf{u}_j)$. This is a typical least square problem, and we solve it for $\mathbf{P}$ using the optimization package *MOSEK*([33]).

If the fitting results don't meet the requirement, we can improve them by refitting after adaptively subdividing cells where large fitting errors occur. Each cell from P can be split into two, four or eight smaller ones, depending on its aspect ratio. Once vertices, faces, and cells are added, Algorithm 1 is employed to refine existing RTP-spline and introduce additional degree-of-freedom for better fitting. Note that Algorithm 1 is originally devised to work on a box domain, it can be however straightforwardly applied to RTP-splines defined on polycube domains, with a minor revision. That is, whenever a new boundary vertex is added, we have to insert a few sub-anchors in addition to the master anchor by following the way described in Section 4.3.3, in order to preserve the restricted boundary on the resulting RTP-splines.

Compared with the number of degrees of freedom (DOFs) in the optimization problem (Equation 8), U normally contains a much greater number of parametric points evenly distributed inside the polycube domain. So the optimization problem is well-posed and the resulting linear equations form a nondegenerate system. If there are too many subdivisions, the increased number of DOFs may lead to degenerate systems. In this case, we will first enlarge U by adding more points on the parametric domain near where subdivisions take place and then recalculate X.

6 Results and Discussion

TABLE 2
Statistics of Volume Fitting.

Models	Data Points	# Control Points	RMS Error $\times 10^{-3}$	Timing (seconds)
Bimba	35511	4543	1.20	31.21
Kitten	60144	3820	1.27	44.53
2-Torus	26384	2888	3.69	20.65
Hand	1502700	9035	0.554	1150
Head	472122	12880	0.291	422.4
Beethoven				
(1st level)	103361	1001	1.80	67.79
(2nd level)	103361	3283	1.34	80.78
(3rd level)	103361	14699	0.718	123.28

A system consisting of volumetric parametrization, RTP-spline construction and data fitting is implemented in C++ and the experiments are carried out on a 3GHz Pentium-IV PC with 4G RAM. Our experimental data include solid models of Bimba, Beethoven, eight (genus 2), kitten (genus 1), hand (5 bifurcations) and head (with brain excavated), which are represented as tetrahedral meshes. We successfully convert them into representations of single-pieced smooth RTP-splines by using the method proposed in this paper. The experimental results are given in Fig. 11.

TABLE 3
Computational costs in calculating blending functions and their derivatives : RTP-splines VS general T-splines. The time includes total computation spent on blending functions values and their derivatives at all sample points. The blending functions used in comparison are defined as $\hat{B}_i(u,v,w) = w_i B_i(u,v,w)$ for RTP-splines, and $\hat{B}_i(u,v,w) = w_i B_i(u,v,w) / \sum_{j=1}^{|\mathcal{B}|} w_j B_j(u,v,w)$ for T-splines respectively.

Model	Sample Points	Polycube Spline			General T-spline		
		$\hat{B}(u,v,w)$	$\hat{B}'(u,v,w)$	$\hat{B}''(u,v,w)$	$\hat{B}(u,v,w)$	$\hat{B}'(u,v,w)$	$\hat{B}''(u,v,w)$
Bimba	2512	0.18s	0.6s	1.12s	0.35s	1.14s	2.62s
Kitten	23076	1.61s	5.21s	9.59s	2.95s	9.75s	23.1s
2-Torus	9768	0.71s	2.42s	4.36s	1.37s	4.43s	10.2s

This step of the RTP-splines construction is efficient and usually takes only a few seconds, which consists of deducing knot vectors, building blending functions, calculating weights and initializing necessary data structures. In all our experiments, this step takes at most 6 seconds (for the Beethoven model at level 3). In contrast, fitting RTP-splines to volumetric datasets is more computationally expensive. The statistics of volumetric fitting are documented in Table 2, where the data points are parameterized on polycube domains, the fitting qualities are measure by RMS errors, and the fitting errors are normalized to the overall sizes of solid models. From Table 2, we find that the volumetric fitting of the RTP-splines can be finished efficiently and yield reasonable results. In addition, RTP-splines enable local subdivision of cells over desired regions to improve fitting qualities. As shown in the Beethoven model: the initial error is 1.80×10^{-3} without subdivisions and is reduced to 7.18×10^{-4} after two levels of subdivisions. The geometric details of the Beethoven model are also gradually revealed with the increasing level of subdivision (see Figure 10).

RTP-spline is semi-standard and hence computing blending functions and their derivatives on it is much more efficient than on traditional T-splines. To prove this, we compared the computational cost on the models Bimba, Kitten and two-hole torus in both kinds of spline representations. To ensure the fairness in the comparisons, we use the same source codes of RTP-splines to compute blending functions and derivatives for traditional T-splines, by including calculation of denominators. The comparison results given in Table 3. As a result, the costs of the calculations of $\hat{B}$, $\hat{B}'$, and $\hat{B}''$ using traditional T-splines are roughly reduced by 47%, 46%, and 58% respectively if RTP-splines are used instead.

We can model other attributes in addition to geometry in RTP-splines by increasing the vector sizes of control points. In one of our experiments, we synthesize a scalar field on the head model, and then successfully recover a single RTP-spline representation of both the geometry and scalar values as shown in Figure 12. Two kinds of scalar fields are involved in the experiment. One is the distance field to both the head surface and the brain surface inside (see Figure 12(d)). The fitting results for the distance field and the corresponding fitting error map are demonstrated in Figure 12(e)(f) respectively. Note that the fitting errors shown here are also normalized RMS errors as the distances are related to the model geometry. The other type of scalar field is a synthesized procedure 3D texture, generated using the fractal sum of Perlin noise [34] as $T(\mathbf{p}) = \sum_{i=1}^{4} \frac{1}{i} noise(i\mathbf{p}), \mathbf{p} \in \mathbb{R}^3$)(see Figure 12(g)). In the experiment, the value of $T(\mathbf{p})$ varies from 0.8 to -1.33. And the absolute RMS fitting error to $T(\mathbf{p})$ is 7.3×10^{-4} (see Figure 12(h)(i)).

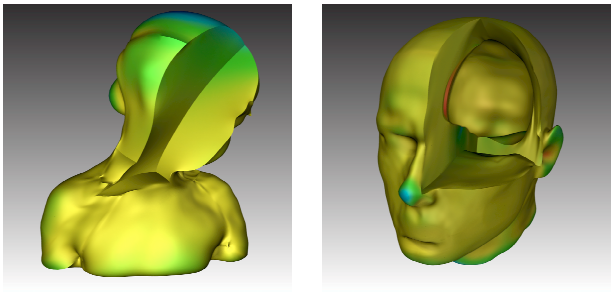

Fig. 9. The RTP-spline function is considered as a deformation function describing the transformation from a polycube to a solid objects. The Jacobians of the deformation gradients are shown in the above pictures, showing the smoothness of the derivatives of the splines.

As a RTP-spline function is continuously and smoothly defined over a polycube, we can evaluate any properties that depends on function values and derivatives anywhere over the domain. If we interpret the RTP-spline function $\mathbf{F}$ obtained from data fitting as a deformation from a polycube to the shape of the fitted solid model, the deformation gradient tensor is $\mathbf{G} = \mathbf{F} \otimes \nabla$ and its Jacobian $det(\mathbf{G})$ measures the volume changes produced by the deformation. In Figure 9, the Jacobian values for the hand and Bimba model are directly evaluated from function value and derivatives of $\mathbf{F}$ and there are no abrupt jumps in color due to the smoothness and continuity of RTP-splines.

Linear Independence of Blending Functions. In this paper, we use the term RTP-spline *blending* functions instead of *basis* functions because whether they are linearly independent is not clear. It has been proven in [35] that linear independence is not guaranteed for general T-splines. It's also pointed out that [35] linear independence can be inherited from a coarse T-mesh after a sequence of refinement only if in each step we insert anchors following certain constraints. However, a similar conclusion has not been revealed on T-lattices for trivariate T-splines, so the linear independence property of RTP-splines remains open.

Presence of linear dependence will not severely impact RTP-splines fitting, which is posed as a linear least square problem. Intuitively, if the refinement in Section 4.3.1 introduces no sub-anchors in addition to those selectively inserted in Section 4.3.3 and Section 4.3.4, degeneracy will not happen. It is still desirable to explore linear independence property of RTP-splines, and/or to have an adaptive modification scheme on RTP-splines construction to ensure linear independency, which is required in certain applications such as isogeometric analysis.

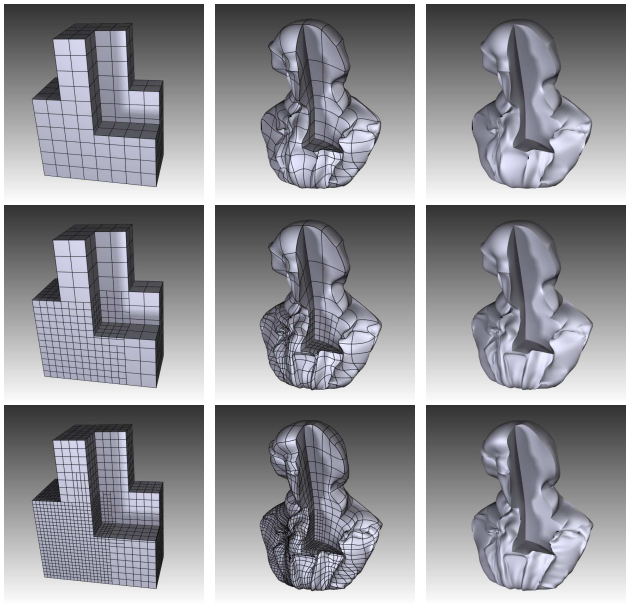

Fig. 10. Adaptive Fitting of Beethoven (from top to bottom: fitting with 0, 1 and 2 levels of subdivisions).

7 Conclusion

In this paper we have proposed the concept and construction algorithm of RTP-splines and presented an effective framework to transform volumetric data (both geometries and associated attributes of solid objects) into representation of RTP-splines. Because of the topological flexibility of the polycube domain, RTP-splines can naturally model solid objects with bifurcations and high genus as a single piece smooth function with a restricted boundary, while ensuring lower parametrization distortion in comparison with traditional splines defined over standard box domains. Our algorithm guarantees that the initially-constructed RTP-splines are semi-standard, so that it enables the efficient computation of spline functions and their derivatives, without any division overhead. The proposed RTP-spline supports local refinement, and a refinement algorithm has been developed to preserve the semi-standardness on the RTP-splines undergoing anchor insertion and local subdivision. The particular restricted boundary requirement of RTP-splines prevents control points from affecting domain regions spanning across nearby boundaries.

We demonstrate the efficacy of our RTP-splines as a powerful solid modeling tool in various experiments. This unified paradigm enables the transformation from discrete solid models (represented by tetrahedral meshes) into continuous RTP-spline representations, accurately modeling both geometry and possibly multi-dimensional attributes.

One unclear property of the RTP-spline is its linear independence, we will explore the constraints during the RTP-spline construction that ensures it. When the linear independence problem is solved, we would also like to explore the isogeometric analysis founded upon RTP-splines. Moreover, the particular polycube domains of RTP-splines can be naturally decomposed into a set of regular structures, which will enable GPU-friendly computing and image-based geometric shape processing.

References

[1] T. W. Sederberg, D. L. Cardon, G. T. Finnigan, N. S. North, J. Zheng, and T. Lyche, "T-spline simplification and local refinement," *ACM Trans. on Graphics*, vol. 23, no. 3, pp. 276–283, 2004.

[2] J. Hua, Y. He, and H. Qin, "Trivariate simplex splines for inhomogeneous solid modeling in engineering design," *Journal of Computing and Information Science in Engineering*, vol. 5, no. 2, pp. 149–157, 2005.

[3] H. Si, "Tetgen: A quality tetrahedral mesh generator and three-dimensional delaunay triangulator," 2005.

[4] X. Zhou and J. Lu, "Nurbs-based galerkin method and application to skeletal muscle modeling," in *Proc. of ACM Symposium on Solid and Physical Modeling*, 2005, pp. 71–78.

[5] T. J. Hughes, J. A. Cottrell, and Y. Bazilevs, "Isogeometric analysis: CAD, finite elements, NURBS, exact geometry, and mesh refinement," *Computer Methods in Applied Mechanics and Engineering*, vol. 194, no. 39-41, pp. 4135–4195, 2005.

[6] T. Martin, E. Cohen, and R. M. Kirby, "Volumetric parameterization and trivariate B-spline fitting using harmonic functions," *Computer Aided Geometric Design*, vol. 26, no. 6, pp. 648–664, 2009.

[7] T. W. Sederberg, J. Zheng, A. Bakenov, and A. Nasri, "T-splines and T-NURCCs," *ACM Trans. on Graphics*, vol. 22, no. 3, pp. 477–484, 2003.

[8] B. Schmitt, A. Pasko, and C. Schlick, "Constructive modeling of FRep solids using spline volumes," in *Proc. of the 6th ACM Symposium on Solid modeling and Applications*, 2001, pp. 321–322.

[9] W. Martin and E. Cohen, "Representation and extraction of volumetric attributes using trivariate splines," in *Proc. of the 6th ACM Symposium on Solid modeling and Applications*, 2001, pp. 234–240.

[10] D. L. Cardon, "T-spline simplification," Master's thesis, Brigham Young University, Provo, UT 84602, USA, 2007.

[11] H. Ipson, "T-spline merging," Master's thesis, Brigham Young University, Provo, UT 84602, USA, 2005.

[12] Y. Bazilevs, V. Calo, J. Cottrell, J. Evans, S. Lipton, M. Scott, and T. Sederberg, "Isogeometric analysis using T-splines," *Computer Methods in Applied Mechanics and Engineering*, vol. 199, no. 5-8, pp. 229–263, 2010.

[13] W. Song and X. Yang, "Free-form deformation with weighted T-spline," *The Visual Computer*, vol. 21, no. 3, pp. 139–151, 2005.

[14] R. Feichtinger, M. Fuchs, B. Jüttler, O. Scherzer, and H. Yang, "Dual evolution of planar parametric spline curves and T-spline level sets," *Computer-Aided Design*, vol. 40, no. 1, pp. 13–24, 2008.

[15] H. Yang and B. Jüttler, "Evolution of T-spline level sets for meshing non-uniformly sampled and incomplete data," *The Visual Computer*, vol. 24, no. 6, pp. 435–448, 2008.

[16] ——, "Meshing non-uniformly sampled and incomplete data based on displaced T-spline level sets," in *Proc. of the IEEE International Conference on Shape Modeling and Applications*, 2007, pp. 251–260.

[17] ——, "3D shape metamorphosis based on T-spline level sets," *The Visual Computer*, vol. 23, no. 12, pp. 1015–1025, 2007.

[18] M. Tarini, K. Hormann, P. Cignoni, and C. Montani, "Polycube-maps," *ACM Trans. on Graphics*, vol. 23, no. 3, pp. 853–860, 2004.

[19] H. Wang, Y. He, X. Li, X. Gu, and H. Qin, "Polycube splines," *Computer Aided Design*, vol. 40, no. 6, pp. 721–733, 2008.

[20] H. Wang, M. Jin, Y. He, X. Gu, and H. Qin, "User-controllable polycube map for manifold spline construction." in *Proceedings of ACM Symp. on Solid and Physical Modeling*, 2008, pp. 397–404.

[21] J. Lin, X. Jin, Z. Fan, and C. Wang, "Automatic polycube-maps," in *Proc. of the 5th International Conference on Geometric Modeling and Processing*, 2008, pp. 3–16.

[22] Y. He, H. Wang, C.-W. Fu, and H. Qin, "A divide-and-conquer approach for automatic polycube map construction," *Computers & Graphics*, vol. 33, no. 3, pp. 369–380, 2009.

[23] Y. Wang, X. Gu, T. F. Chan, P. M. Thompson, and S. T. Yau, "Volumetric harmonic brain mapping," in *Proc. of IEEE international Symposium on Biomedical imaging.*, 2004, pp. 1275–1278.

[24] X. Li, X. Guo, H. Wang, Y. He, X. Gu, and H. Qin, "Meshless harmonic volumetric mapping using fundamental solution methods," *IEEE Trans. on Automation Science and Engineering*, vol. 6, no. 3, pp. 409–422, 2009.

[25] T. Martin, E. Cohen, and M. Kirby, "Volumetric parameterization and trivariate B-spline fitting using harmonic functions," in *Proc. of ACM Symposium on Solid and Physical Modeling*, 2008, pp. 269–280.

[26] T. Martin and E. Cohen, "Volumetric parameterization of complex objects by respecting multiple materials," *Computers & Graphics*, vol. 34, no. 3, pp. 187–197, 2010.

[27] J. Xia, Y. He, X. Yin, S. Han, and X. Gu, "Direct-product volumetric parameterization of handlebodies via harmonic fields," in *Proc. of Shape Modeling International Conference*, 2010, pp. 3–12.

[28] J. Xia, Y. He, S. Han, C.-W. Fu, F. Luo, and X. Gu, "Parameterization of star-shaped volumes using green's functions," in *Proc. of the 6th International Conference on Geometric Modeling and Processing*, 2010, pp. 219–235.

[29] C.-Y. Yao, H.-K. Chu, T. Ju, and T.-Y. Lee, "Compatible quadrangulation by sketching," *Computer Animation & Virtual Worlds*, vol. 20, no. 2-3, pp. 101–109, 2009.

[30] X. Li, X. Guo, H. Wang, Y. He, X. Gu, and H. Qin, "Harmonic volumetric mapping for solid modeling applications," in *Proc. of ACM Symposium on Solid and Physical Modeling*, 2007, pp. 109–120.

[31] X. Li, H. Xu, S. Wan, Z. Yin, and W. Yu, "Feature-aligned harmonic volumetric mapping using MFS," *Computers & Graphics*, vol. 34, no. 3, pp. 242–251, 2010.

[32] X. Li, Y. Bao, X. Guo, M. Jin, X. Gu, and H. Qin, "Globally optimal surface mapping for surfaces with arbitrary topology," *IEEE Trans. on Visualization and Computer Graphics*, vol. 14, no. 4, pp. 805–819, 2008.

[33] "Mosek, http://www.mosek.com/."

[34] K. Perlin, "An image synthesizer," *SIGGRAPH Computer Graphics*, vol. 19, no. 3, pp. 287–296, 1985.

[35] A. Buffa, D. Cho, and G. Sangalli, "Linear independence of the T-spline blending functions associated with some particular T-meshes," *Computer Methods in Applied Mechanics and Engineering*, vol. 199, no. 23-24, pp. 1437–1445, 2010.

Kexiang Wang received the BS and MS degrees in computer science from the University of Science and Technology of China in 1998 and 2001, respectively and the PhD degree in computer science from Stony Brook University (SUNY) in 2010. He currently works as a data analyst at Renaissance Technologies, LLC.

Xin Li is an assistant professor of Department of Electrical and Computer Engineering and Center for Computational and Technology at Louisiana State University. He obtained his BS in Computer Science from University of Science and Technology of China, MS and PhD in Computer Science from Stony Brook University (SUNY). His research interests include geometric modeling, computer graphics, vision, visualization. His recent works include curve, surface and volumetric shape mapping/matching, and their applications in digital forensics, computational medicine, and robotics. He is a member of IEEE Computer Society. For more information, visit http://www.ece.lsu.edu/xinli.

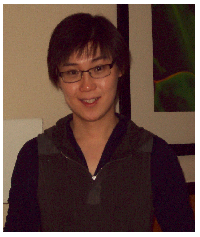

Bo Li is a PH.D candidate in Department of Computer Science at Stony Brook University. He received his B.S. degree in Computer Science from ZhongShan University (Sun Yet-sen University). His research interests includes computer graphics, geometric modeling, computer-aided geometric design (CAGD), physical animation/simulation, and visualization. For more details, please visit http://www.cs.stonybrook.edu/ bli

Huanhuan Xu is a PhD candidate in Department of Electrical and Computer Engineering at Louisiana State University. She obtained the M.Sc. degree in University of Science Technology of China in 2006. Her research interests include 3D computer graphics, geometric modeling, image processing, and pattern recognition.

Hong Qin is a Professor of Computer Science in Department of Computer Science at State University of New York at Stony Brook (Stony Brook University). He received his B.S. degree and his M.S. degree in Computer Science from Peking University. He received his Ph.D. degree in Computer Science from the University of Toronto. In 1997, Professor Qin was awarded NSF CAREER Award from the National Science Foundation (NSF). He was also a recipient of Honda Initiation Award, and Alfred P. Sloan Research Fellow by the Sloan Foundation. Professor Qin served as the general Co-Chair for Computer Graphics International 2005 (CGI'2005). He was the Conference Co-Chair for ACM Solid and Physical Modeling Symposium in 2007. Currently, he is an associate editor for IEEE Transactions on Visualization and Computer Graphics (IEEE TVCG), The Visual Computer, and Journal of Computer Science & Technology. In 2008, he served as the Conference Chair for for ACM Solid and Physical Modeling Symposium and IEEE International Conference on Shape Modeling and Applications. His research interests include geometric and solid modeling, graphics, physics-based modeling and simulation, computer aided geometric design, human-computer interaction, visualization, and scientific computing. For more details, please visit http://www.cs.sunysb.edu/ qin

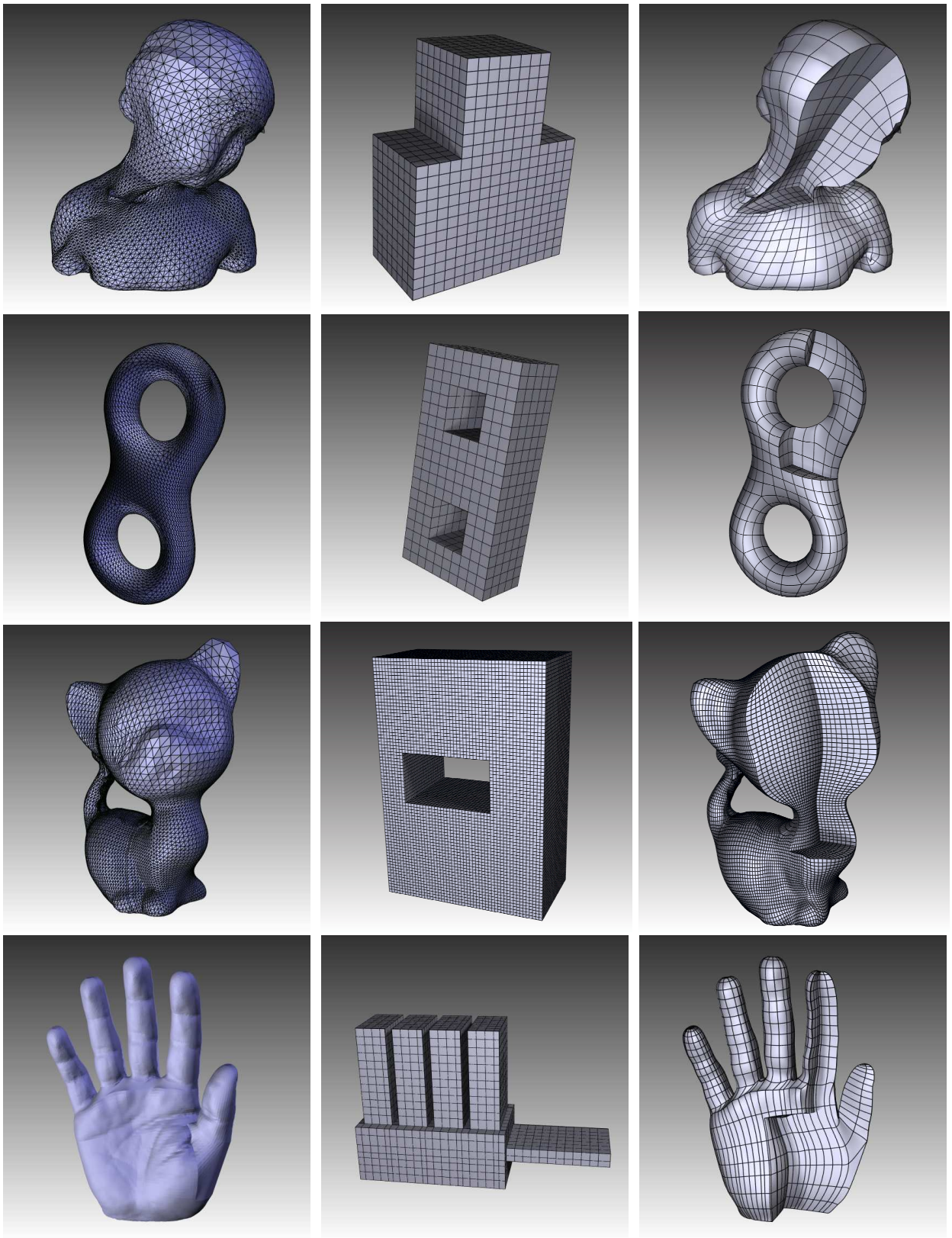

Fig. 11. From left to right, original solid models represented by tetrahedral meshes, polycube domains of RTP-splines, and hexahedral meshes rendered from RTP-spline functions. (The edges of the hand tetrahedral model are omitted on purpose due to their extraordinary numbers.)

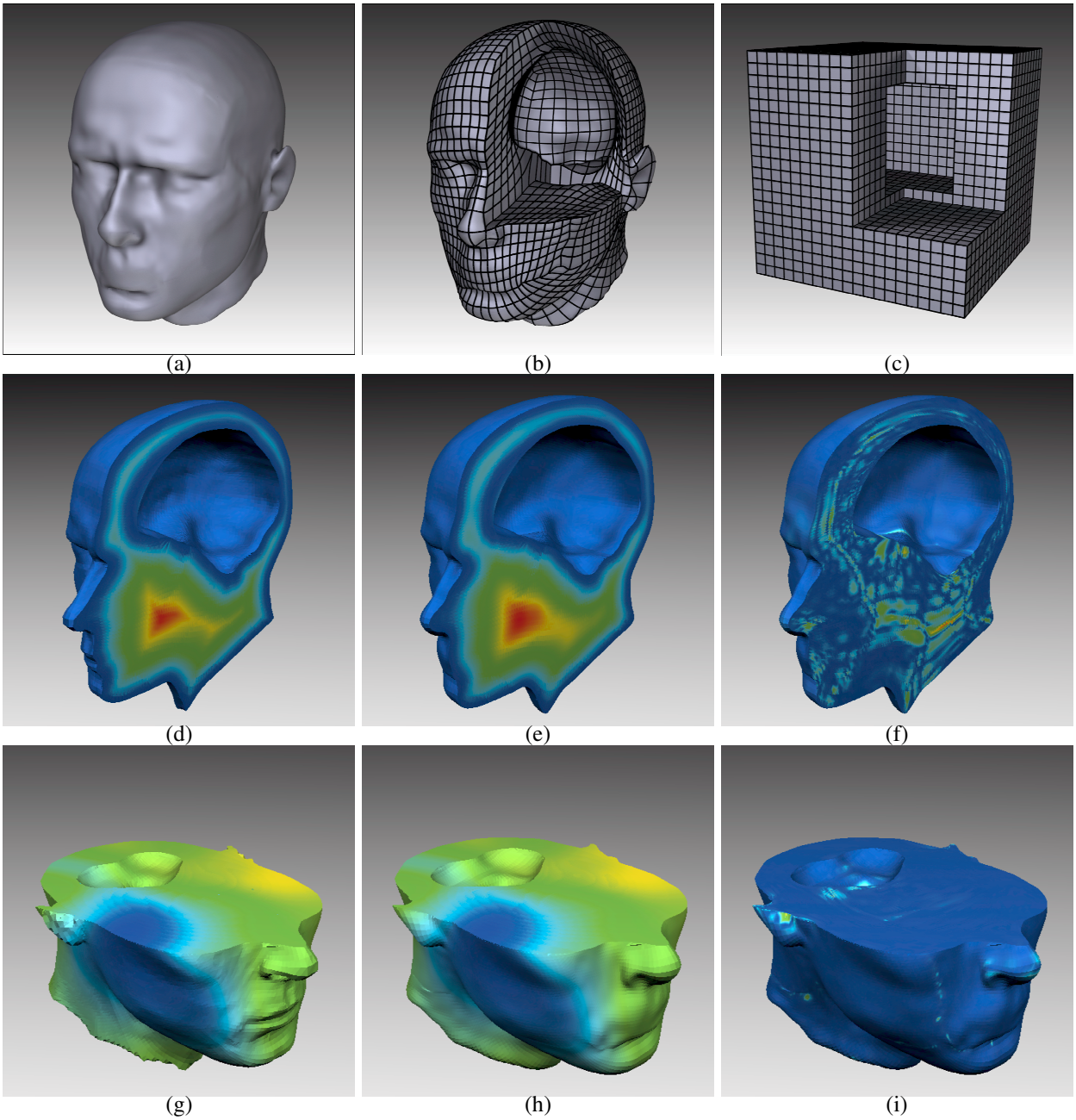

Fig. 12. Fitting results for the head model associated with synthesized scalar field (red denotes high value while blue denotes low value). (a) polycube in parametric domain, (b,c) are the volumetric meshes reproduced from fitted RTP-splines, (d) synthesized distance field texture, (e) texture generated from the fitted RTP-spline, (f) fitting error map, where the maximum error is $0.92 * 10^{-2}$ and the average is $6.0 * 10^{-4}$; (g) texture synthesized as a Perlin noise function. (h,i) show the fitting errors and the error map respectively. The maximum fitting error for noise texture is 0.066 and the average is $7.3 * 10^{-4}$.